The Role of Zn Ions in the Structural, Surface, and Gas-Sensing Properties of SnO_2:Zn Nanocrystals Synthesized via a Microwave-Assisted Route

Journal Article

Author(s):
da Silva, Luís F.; Lucchini, Mattia A.; Catto, Ariadne C.; Avansi Jr., Waldir; Bernardini, Sandrine; Aguir, Khalifa; Niederberger, Markus; Longo, Elson

Publication date:
2023-12-26

Permanent link:
https://doi.org/10.3929/ethz-b-000650447

Originally published in:
Sensors 24(1), https://doi.org/10.3390/s24010140

sensors

MDPI

Article

The Role of Zn Ions in the Structural, Surface, and Gas-Sensing Properties of SnO_2:Zn Nanocrystals Synthesized via a Microwave-Assisted Route

Luís F. da Silva [1,2,*], Mattia A. Lucchini [1], Ariadne C. Catto [3], Waldir Avansi Jr. [2], Sandrine Bernardini [4], Khalifa Aguir [4], Markus Niederberger [1] and Elson Longo [3]

[1] Laboratory for Multifunctional Materials, Department of Materials, ETH Zürich, 8093 Zürich, Switzerland; mattia.a.lucchini@gmail.com (M.A.L.); markus.niederberger@mat.ethz.ch (M.N.)
[2] Laboratory of Nanostructured Multifunctional Materials, Federal University of São Carlos, São Carlos 13565-905, Brazil; w_avansi@yahoo.com.br
[3] Center for the Development of Functional Materials, Federal University of São Carlos, São Carlos 13565-905, Brazil; ade.catto@gmail.com (A.C.C.); elson.liec@gmail.com (E.L.)
[4] Aix Marseille Univ, CNRS, IM2NP, 13397 Marseille, France; sandrine.bernardini@im2np.fr (S.B.); khalifa.aguir@im2np.fr (K.A.)
* Correspondence: lfsilva83@gmail.com

Abstract: Although semiconducting metal oxide (SMOx) nanoparticles (NPs) have attracted attention as sensing materials, the methodologies available to synthesize them with desirable properties are quite limited and/or often require relatively high energy consumption. Thus, we report herein the processing of Zn-doped SnO_2 NPs via a microwave-assisted nonaqueous route at a relatively low temperature (160 °C) and with a short treatment time (20 min). In addition, the effects of adding Zn in the structural, electronic, and gas-sensing properties of SnO_2 NPs were investigated. X-ray diffraction and high-resolution transmission electron microscopy analyses revealed the single-phase of rutile SnO_2, with an average crystal size of 7 nm. X-ray absorption near edge spectroscopy measurements revealed the homogenous incorporation of Zn ions into the SnO_2 network. Gas sensing tests showed that Zn-doped SnO_2 NPs were highly sensitive to sub-ppm levels of NO_2 gas at 150 °C, with good recovery and stability even under ambient moisture. We observed an increase in the response of the Zn-doped sample of up to 100 times compared to the pristine one. This enhancement in the gas-sensing performance was linked to the Zn ions that provided more surface oxygen defects acting as active sites for the NO_2 adsorption on the sensing material.

Keywords: SnO_2; zinc; non-aqueous synthesis; microwave route; local structure; surface properties; chemoresistors

Citation: da Silva, L.F.; Lucchini, M.A.; Catto, A.C.; Avansi Jr., W.; Bernardini, S.; Aguir, K.; Niederberger, M.; Longo, E. The Role of Zn Ions in the Structural, Surface, and Gas-Sensing Properties of SnO_2:Zn Nanocrystals Synthesized via a Microwave-Assisted Route. *Sensors* **2024**, *24*, 140. https://doi.org/10.3390/s24010140

Academic Editor: Eduard Llobet

Received: 13 November 2023
Revised: 14 December 2023
Accepted: 15 December 2023
Published: 26 December 2023

1. Introduction

Climate change has been the main topic covered in scientific forums to find groundbreaking strategies to minimize the influence of human activities on global environmental problems. Industrial activities and the burning of fossil fuels have been primarily responsible for the release of various gases into the atmosphere [1–4]. Some of these gaseous species, in addition to contributing to the greenhouse effect, are also harmful to human health, such as NO_2, O_3, and CO [2,5,6]. Unfortunately, people who live and/or work near these pollutants are more likely to contract certain diseases, such as respiratory and cardiovascular ones, and even cancer. Recently, the World Health Organization (WHO) reported that atmospheric pollution has been responsible for the death of approximately 7 million people worldwide per year [2,4,7].

Nitrogen dioxide (NO_2) is a toxic gas, and exposure to it can cause inflammation of the airways, asthma, and other respiratory sicknesses (e.g., coughing and difficulty in breathing) [6,8,9]. The largest sources of NO_2 gas emissions are mainly linked to the

burning of fossil fuels [1,10,11]. The United States Environmental Protection Agency (US EPA) recommends a NO_2 level of 0.1 parts per million (ppm) for a maximum of 1 h of exposure [8]. For instance, the air pollution levels in Europe have been reduced over the last few decades; even so, NO_2 gas has been responsible for thousands premature deaths every year [12].

Gas sensors, particularly chemoresistors based on SMOx NPs (semiconductor metal oxide nanoparticles) detect NO_2 through a change in electrical resistance when exposed to the gas. When NO_2 interacts with the surface of the sensor, it causes a change in the conductance of the semiconductor metal oxide, leading to a measurable change in resistance. This change is then converted into an electrical signal, allowing for the detection and quantification of NO_2. The sensors are designed to be sensitive, selective, and operational at room temperature, making them suitable for various applications such as environmental monitoring and industrial safety [13,14]. They are designed to provide accurate and reliable monitoring of NO_2 levels, with a wide range of detection capabilities, from parts per billion (ppb) to parts per million (ppm).

These data reveal the need for the development of efficient sensing devices that could make the monitoring of air pollution levels more accessible and reliable, especially for detecting sub-ppm levels. Among the devices applied for the detection of hazardous gas, resistive "chemoresistors" are gas sensors which have been used to detect a variety of analytes, such as NO_2 gas. Gas sensors based on SMOx NPs have been outstanding due to their high sensing activity, linked to their high-surface area that favors the catalytical processes between the SMOx surface and analyte [1,15–19].

Among the traditional SMOx, tin dioxide (SnO_2) is one of the most studied sensing materials due to its sensitivity to a variety of analytes [20–23]. It is an n-type SMOx with an energy gap of ca. 3.6 eV (at 300 K) which makes it also promising for photocatalysis and energy generation [24–29].

One well-known way to improve the sensing properties of SnO_2 is to add certain dopants, such as transition metals and noble metals [16,30–35]. Previous studies have demonstrated that an extrinsic doping/co-doping strategy has a significant influence on the sensing performance (e.g., sensitivity, selectivity, and working temperature) [16,17,30,36,37]. Vallejos and co-workers prepared Au-decorated SnO_2 nanorods via aerosol-assisted chemical vapor deposition to be applied as gas sensors. The authors found an enhancement in the sensitivity and selectivity toward H_2 compared to the bare sample [30]. In a previous study, we observed an increase in ozone sensor response of ZnO thin films with Co content. This enhancement in the gas-sensing properties was attributed to the presence of oxygen vacancies, which facilitated ozone adsorption [17].

Concerning the effect of Zn addition on the gas-sensing performance of SnO_2, some investigations have reported promising data, as illustrated in Table 1. These studies have reported that the addition of Zn ions to SnO_2 may modify its electronic structure, increasing the surface oxygen defects due to charge compensation, which may affect the sensing performance [25,37,38].

Table 1. Gas-sensing performance of Zn-doped SnO_2 synthesized by different methodologies.

Synthesis Method	Temperature/Time of Synthesis	Target Gas	Gas Level Detected * (ppm)	Working Temperature (°C)	Reference
Hydrothermal	180 °C/16 h	Glycol	5.0	240	[38]
Spray pyrolysis	350 °C/**	Formic Acid	50.0	350	[39]
Hydrothermal	200 °C/12 h	Ethanol	40.0	250	[40]
Precipitation	550 °C/2 h	Ethanol	2.0	240	[41]
Hydrothermal	180 °C/24 h	Triethylamine	100.0	70	[37]
Hydrothermal	190 °C/ 12 h	NO_2	1.0	350	[42]
Hydrothermal	140 °C/24 h	NO_2	0.35	200	[43]
Microwave-assisted	160 °C/ 20 min	NO_2	0.10	150	Present study

* Minimum gas level, experimentally detected/** deposition time not provided.

Regarding the synthesis method, nonaqueous routes have attracted attention in terms of obtaining materials with diverse functional properties in a controlled and reproductive way [44,45]. The microwave-assisted nonaqueous synthesis of organic solvents under the exclusion of water is able to overcome some of the major limitations of aqueous systems. The main advantages of this route are the simplicity, short synthesis times (few minutes), and relatively low temperatures (<200 °C) [45,46], mainly when compared to the data in Table 1. In the gas-sensing area, we have previously reported the potential of the microwave-assisted route to obtain ZnO/SnO_2 nanoheterostructures applied as ozone gas sensors. The experiments demonstrated that heterostructures were promising for detecting ozone gas under UV-light stimulation [47].

Motivated by these considerations, we conducted a detailed investigation of the effects of Zn ions on the structural, surface, and NO_2 gas-sensing properties of SnO_2 NPs synthesized via the microwave-assisted nonaqueous method. The properties of Zn-doped SnO_2 NPs were studied by X-ray diffraction (XRD), X-ray absorption near-edge structure spectroscopy (XANES), high-resolution transmission electron microscopy (HRTEM), and X-ray photoelectron spectroscopy (XPS). The gas-sensing experiments demonstrated good sensing activity at a mild temperature (150 °C), which could further be improved by increasing the Zn content. In addition, the Zn-doped nanocrystals revealed high stability of their NO_2 sensing performance under different humidity levels.

2. Experimental

2.1. Reagents

Zn (II) acetylacetonate hydrate (99.995%), Sn (IV) chloride (99.99%), toluene (99%) benzyl alcohol (99.8%), acetylacetonate (99.5+%), hexyl alcohol (98%), and 1,3-propanediyl (99.5+%) were all purchased from Aldrich and used as-received without further purification.

2.2. Synthesis Procedure

Pristine SnO_2 and Zn-doped SnO_2 NPs (Zn/(Zn + Sn) = 5 and 30 mol %) were synthesized using a microwave-assisted nonaqueous method in a CEM Discover reactor operating at a frequency of 2.45 GHz. The synthesis of the Zn-doped SnO_2 samples was performed by adding 12.3 mmol of tin tetrachloride and zinc acetylacetonate to 10 mL of toluene and then 30 mL of benzyl alcohol was added to the solution. Concerning the undoped SnO_2 sample, the procedure was similar except for the addition of a zinc precursor. Thereafter, the reaction mixture was transferred into a 35 mL glass tube and sealed with a Teflon cap. The microwave-assisted treatment was performed for 20 min at 160 °C, maintaining the reaction mixture in continuous stirring. The precipitate was separated from the liquid phase by centrifugation, washed three times with ethanol, and then dried overnight at 60 °C. The Zn-doped samples were labeled as SnZn1 (5 mol % Zn) and SnZn2 (30 mol % Zn).

2.3. Characterization Techniques

X-ray diffraction (XRD) patterns were measured using a Shimadzu XRD 6100 (Shimadzu Corporation, Kyoto, Japan) diffractometer with a monochromatic Cu Kα source, collected at room temperature, in a continuous scan mode with a speed of 2° min^{-1} and a step of 0.02°. The morphological properties were analyzed using a field emission scanning electron microscope (FE-SEM, Supra35, ZEISS Company, Jena, Germany) and a high-resolution transmission electron microscope (HRTEM, TECNAI G2 F30, FEI Company, Hillsboro, OR, USA) operating at 200 kV. The mean crystal size was estimated from the analysis of the TEM images through the measurement of approximately 100 NPs. X-ray absorption near-edge spectroscopy (XANES) experiments were carried out at the Brazilian Synchrotron Light Laboratory. The experiments were carried out at the Zn K- and Sn-L3 edges at room temperature using a flat Si(111) double crystal monochromator. The processing and analysis of XANES spectra were performed using the MAX software package [48]. XPS analysis was performed on a Thermo Scientific K-Alpha spectrometer using a monochromatic Al Kα source. The as-obtained data were analyzed using Casa

XPS software 2.3.25 (Casa Software Ltd., Teignmouth, Devon, UK), and the spectra were calibrated using the C 1s line (284.8 eV) of the adsorbed carbon on the sample surface.

2.4. Gas-Sensing Experiments

The detailed procedure of the preparation of sensing devices is described in the Supporting Information. The gas-sensing experiments were carried out in a dynamic chamber that allowed us to control the operating temperature and the gas concentrations by using a set of mass flow controllers. Our workbench allowed exposure of the samples to distinct NO_2 levels, ranging from 0.1 to 2.0 ppm. The total gas flow was kept equal to 500 SCCM. The applied DC voltage was kept constant (1 V), while the electrical resistance was monitored using a sourcemeter (model 2540, Keithley Instruments, Cleveland, OH, USA). Further information can be found in our previous papers [17,49,50]. The sensor response (S) was estimated following the procedure reported elsewhere [51].

The sensing performance of the Zn-doped nanocrystals in ambient moisture and with a reducing gas (here, CO gas) was investigated in another chamber (piezo-driven probe model, NEXTRON company; Busan, Republic of Korea). This chamber was connected to a system that allowed the control of temperature, relative humidity (% RH; from 0 to 40%), and target gas concentration. For the sake of comparison, the performance of the sample with NO_2 and CO gases was evaluated under the same conditions (e.g., sensing chamber, %RH, operating temperature, and gas flow).

3. Results and Discussion

3.1. Characterization of Zn-Doped SnO_2 Nanocrystals

XRD patterns of the doped and undoped SnO_2 samples are presented in Figure 1. All reflections were indexed to a tetragonal SnO_2 phase, in accordance with JCDPS file #41-1445. It should be mentioned that no peaks related to Zn-rich phases were identified, indicating that Zn ions were homogenously incorporated into the SnO_2 lattice. Furthermore, the slight broadening of the XRD peak with increasing Zn content can be linked to the reduction in crystallographic domains. The average crystallite size was estimated from the FWHM of the (110) XRD peak using Scherrer's equation, and the obtained values were 3.2 nm (SnO_2), 3.0 nm (SnZn1), and 2.6 nm (SnZn2). Wang and co-workers observed a similar tendency for Zn-doped SnO_2 nanostructures obtained via a hydrothermal treatment, attributing this peak enlargement to the reduction in crystallinity and crystal size [37].

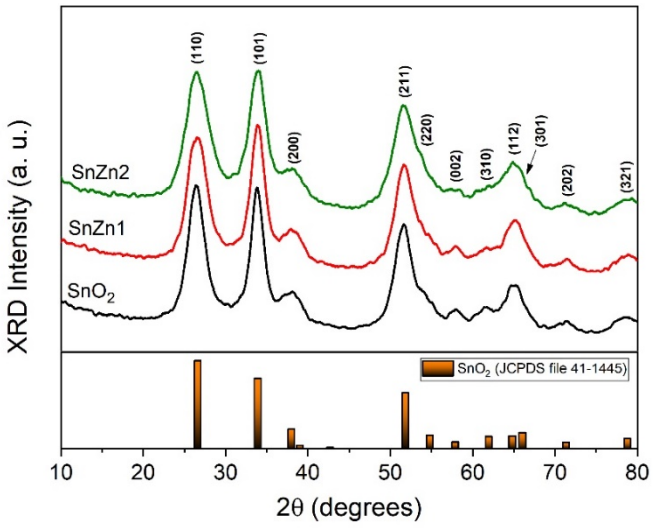

Figure 1. XRD patterns of the undoped and Zn-doped SnO_2 NPs. At the bottom, the vertical bars correspond to the data obtained from the JCPDS file #41-1445.

Figure 2 presents the TEM analysis of pristine SnO_2 and SnZn2, where it can be observed that the spherical morphology of both samples was quite similar, even for the Zn-doped sample, with an average crystal size of 7 nm. HRTEM images, the inset of the respective TEM images, show that the distance between the planes was about 0.34 nm, corresponding to the (110) crystallographic plane of the tetragonal SnO_2, in accordance with the XRD data. The HRTEM images present agglomerated NPs, indicating a coalescence between particles (illustrated by a red arrow) which can be related to the crystal growth mechanism [52–54]. This is expected as previous studies have reported that the oriented attachment mechanism plays an important role in SnO_2 synthesis in hydrothermal conditions [52,55].

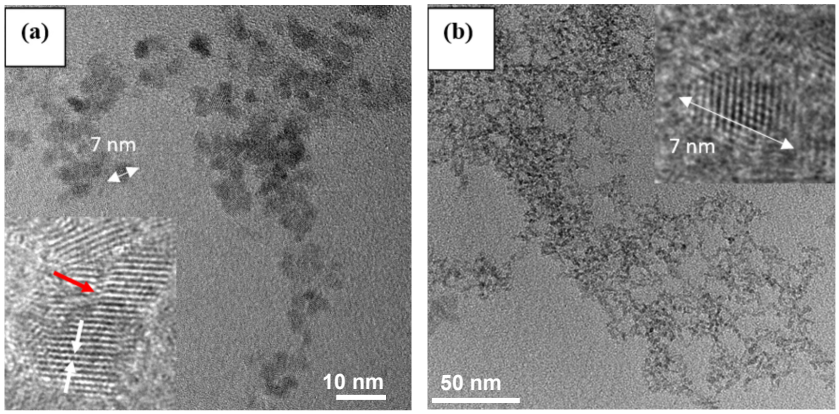

Figure 2. TEM images of selected samples: (**a**) pristine SnO_2 and (**b**) SnZn2 NPs. Inset shows the HRTEM images of their respective samples. (Left) White arrows indicate the atomic distance, and red arrow the coalescence between particles. (Right) White arrows indicate the nanocrystal size.

To investigate the electronic structure of the short-range order of Zn-doped SnO_2 NPs, XANES spectra were collected at the Sn-L3 and Zn-K edges, as displayed in Figure 3. For the sake of comparison, commercial micrometric powders (ZnO and SnO_2) were used as references. XANES spectra at the Sn-L3 edge present three electronic transitions (labeled as P1, P2, and P3), as shown in Figure 3a. The physical origin of these peaks corresponds to electronic transitions from $2p_{3/2}$ to $5s_{1/2}$ and $nd_{5/2}$ levels [28,56]. It can be seen that the pristine SnO_2, SnZn1, and SnZn2 spectra are quite similar to each other, presenting less significant oscillations compared to the reference sample. This feature reveals that these samples have a low short-range order around the Sn atoms that can be attributed to the rapid crystallization provided by the microwave-assisted route. Regarding the Zn addition, no significant influence on the short-range structure of the SnO_2 samples was observed within the zinc content evaluated here.

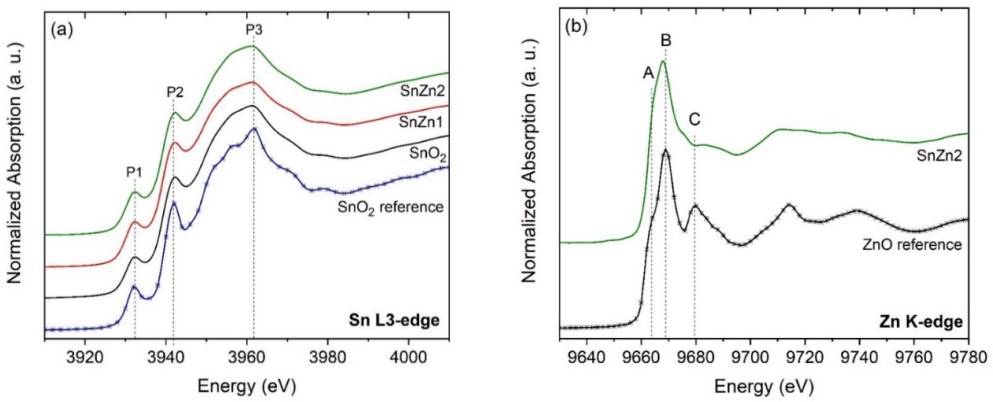

Figure 3. XANES spectra of undoped and Zn-doped SnO_2 NPs. (**a**) Sn L3- and (**b**) Zn-K edge. For the sake of comparison, the spectra of commercial samples are inserted in panels (**a**,**b**).

Figure 3b illustrates the Zn K-edge spectra of SnZn2 and the reference ZnO. Three electronic transitions are visible in the spectra, labeled as A, B, and C. Regarding the electronic transitions A and B, they are attributed to the 1s to 4p transition, and the C transition is due to multiple scattering contributions [17,57]. The analysis of both spectra showed that they differ from each other, especially in the post-edge region between 9670 and 9780 eV. This means that the chemical environment of Zn atoms in SnO_2 samples is not the same as in ZnO, suggesting their homogeneous incorporation in the SnO_2 network. Thus, XANES and XRD analyses allow us to affirm that the addition of Zn ions did not favor the clustering of ZnO (at both long-and short-range) in the Zn-doped SnO_2 nanocrystals.

XPS analysis was carried out to further characterize the pristine SnO_2 and Zn-doped SnO_2 samples and illustrate their surface compositions and electronic states. In the XPS survey spectra of these samples, Figure S2a, the Sn and O were found to be the predominant elements, whilst the Zn was present only in the doped samples, as expected. The quantification of peaks from survey spectra revealed that the Zn atom percentages (at%) were 0.6% and 2.0% for the SnZn1 and SnZn2 samples.

Figure S2b shows the Sn 3d high-resolution XPS spectra, in which the Sn $3d_{5/2}$ and Sn $3d_{3/2}$ peaks were located at 486.6 and 495.0 eV, confirming the presence of Sn^{4+} in all samples. No significant shift in the Sn $3d_{5/2}$ and Sn $3d_{3/2}$ peaks positions with Zn addition was observed, indicating that the zinc addition did not affect the local electronic structure of Sn. From the high-resolution Zn 2p XPS spectra of the Zn-doped SnO_2 samples, Figure S2c, two symmetrical peaks were identified at binding energies of 1022.7 and 1045.8 eV, with a spin-orbit splitting of 23.1 eV, corresponding to Zn $2p_{3/2}$ and $Zn2p_{1/2}$ [58].

Regarding the high-resolution O 1s spectra, Figure 4a, a very asymmetric peak was found that indicates the presence of different oxygen species. These spectra were deconvoluted into two Gaussian–Lorentzian components, labeled as O_I and O_{II}. The main component at 530.2 eV (O_I) was typical of lattice oxygen anions bound to the metal cations, whilst the second component (O_{II}) was linked to hydroxyls and adsorbates [23,37,59,60]. From the O 1s high-resolution spectra, the relative percentage area of the O_{II} component was approximately 38.7% (SnO_2), 39.5% (SnZn1), and 49.3% (SnZn2), indicating that Zn addition increased slightly the concentration of hydroxyls on the surface of the samples. In addition, the metal-to-oxygen ratios (metal/oxygen) of the pristine and Zn-doped samples were also estimated from survey spectra only considering the metal–oxygen bond in O 1s spectra (530.2 eV), and the obtained data are displayed in Figure 4b. The analysis of this figure reveals a tendency to increase the metal/oxygen ratio with zinc content. Note that a stoichiometric sample (SnO_2) must present a metal/O ratio of 0.5, respectively. Thus, the behavior observed in Figure 4b reveals that samples prepared via the microwave-assisted nonaqueous route are oxygen deficient, and the zinc addition into the SnO_2 network favors the enhancement of surface oxygen defects, here induced by the partial substitution of Zn^{2+} by Sn^{4+} ions. Wang and co-workers using experimental and theoretical approaches also demonstrated that the increase in Zn content favored the formation of oxygen vacancies in SnO_2 nanostructures [37].

3.2. Gas-Sensing Measurements

The gas-sensing performances of the pristine SnO_2, SnZn1, and SnZn2 samples were evaluated for NO_2 gas. To find the best working temperature of the samples, they were exposed to 1 ppm of NO_2 with a heating temperature under the sensors varying from 100 to 300 °C, Figure 5. From the analysis of the curves, the highest responses were achieved at around 150 °C for the Zn-doped samples. At this temperature, the response of the SnZn2 sample was around 25 times higher than that of SnZn1 and 100 times higher than the pristine sample. The observed order of sensing performance was SnZn2 > SnZn1 > SnO_2, demonstrating that the Zn addition improved the sensitivity to NO_2 gas. This enhancement can be linked to the addition of Zn ions into the SnO_2 nanocrystals which favored the formation of surface oxygen defects, as above-mentioned. Many studies have highlighted the importance of oxygen defects for improving the sensitivity of SMOx [25,61–63]. Thus,

both Zn ions and surface oxygen defects exert a positive influence on the sensing activity of SnO_2 NPs, acting as active sites for NO_2 sensing reactions. Some researchers have reported that nanosized features and the presence of unsaturated cations and oxygen defects may facilitate the interaction of the analyte at the MOX surface, thus increasing its sensitivity [16,64,65].

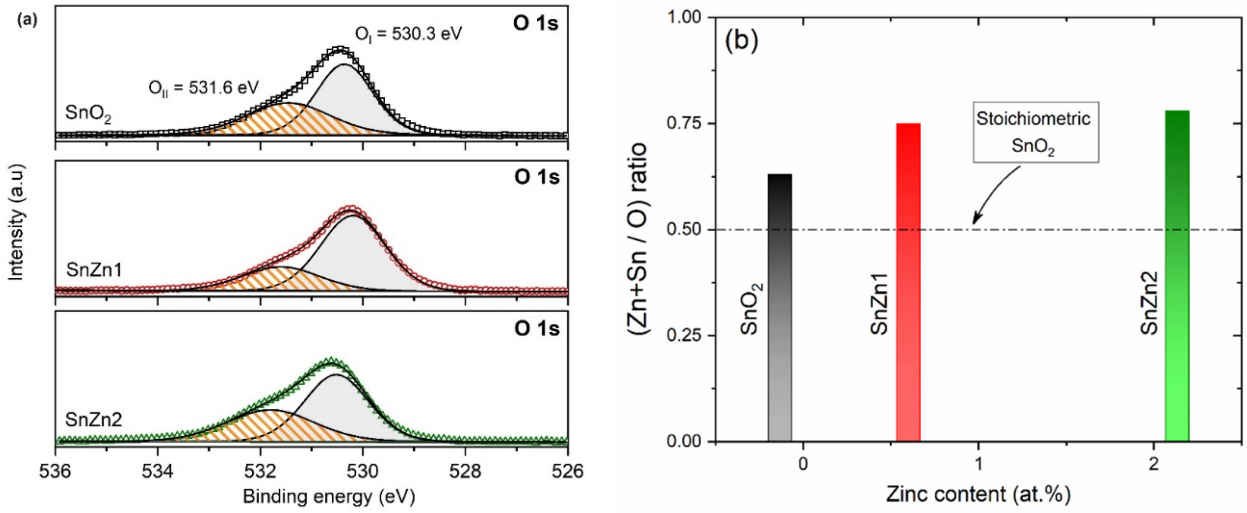

Figure 4. O1 s XPS spectra of the pristine SnO_2, SnZn1, and SnZn2 NPs. (**a**) High-resolution scan and (**b**) variation in (metal/oxygen) ratio as a function of zinc content.

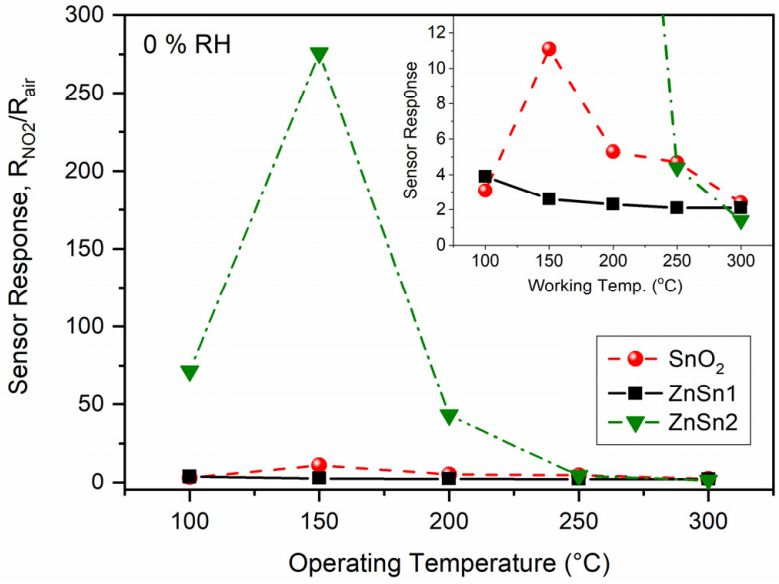

Figure 5. Sensor response of pristine and Zn-doped SnO_2 NPs exposed to 1 ppm NO_2 at different working temperatures. The inset shows in detail the response of SnO_2 and SnZn1 samples. All measurements were performed under dry air (0% RH).

Considering the superior performance of SnZn2 to detect NO_2 gas, it was further investigated at different NO_2 levels ranging from 0.1 to 2 ppm at a working temperature of 150 °C. Figure 6a reveals that this sample was sensitive to all of these levels, with no evidence of saturation. It should be mentioned that these results demonstrate the practical feasibility of Zn-doped SnO_2 NPs as a sensing material since NO_2 gas is harmful to human health in concentrations higher than 0.1 ppm [8,66]. This figure also depicts the good repeatability of the response and recovery of the SnZn2 sample which was able to detect low concentrations even after consecutive exposure cycles.

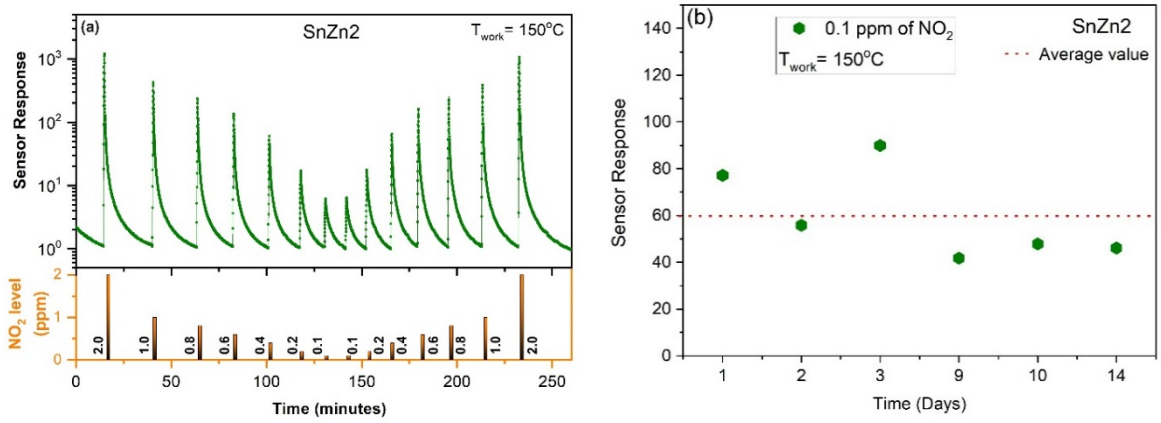

Figure 6. (**a**) Gas-sensing performance of SnZn2 at 150 °C exposed to 0.1 to 2.0 ppm of NO_2 gas. (**b**) Long-term stability of this sample upon exposure to 0.1 ppm of NO_2 gas for a period of approximately 2 weeks. All measurements were performed under dry air (0% RH).

The long-term stability of SnZn2 was also evaluated, exposing it repeatedly to 0.1 ppm of NO_2 gases over 14 days at an operating temperature of 150 °C, as seen in Figure 6b. It can be noted that the sample was able to detect NO_2 gas over the whole period, revealing that its surface remains active after several exposure cycles.

The influence of relative humidity on the NO_2 sensing performance was also investigated. To this end, the SnZn2 NPs were kept at 150 °C and then exposed to 0.2, 0.25, 0.5, 0.7, and 1 ppm of NO_2 gas under different relative humidity values (0, 20, and 40% RH). It can be seen that the NO_2 sensor response was enhanced with increasing relative humidity, as shown in Figure 7a. Note that the sample exhibited high repeatability of its response, confirming its reliability even under ambient moisture, as demonstrated by the nine exposure cycles displayed in Figure 7b.

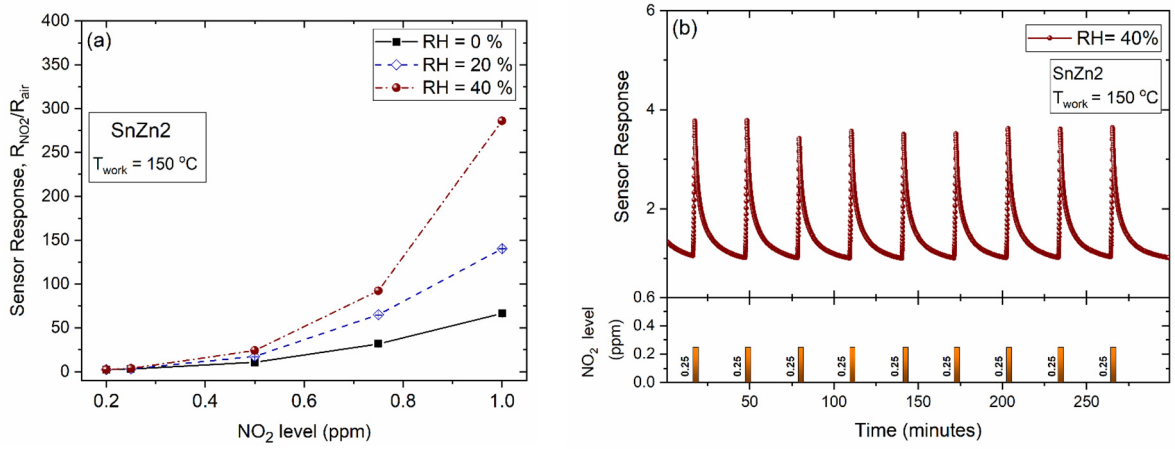

Figure 7. Sensor response of SnZn2 at 150 °C (**a**) exposed to different NO_2 levels under different relative humidity and (**b**) exposed to a sequence of cycles of 0.25 ppm of NO_2 under 40% RH.

According to the findings, the sensor response of SnZn2 to 1 ppm NO_2 increased from S = 66.4 ± 0.4 (RH = 0%) to S = 285.9 ± 0.4 (RH = 40%). A low interference of humidity on the sensing performance is a desirable characteristic in the development of sensing materials [16,66–70]. Several investigations demonstrate that the presence of moisture in the ambient may impair the sensing activity [51,68,71,72]. In 2021, we reported that the sensing response of α-Fe_2O_3 to BTEX gases (Benzene, Toluene, Ethylbenzene, and Xylenes) was reduced as a function of humidity level [51]. This negative effect was linked to the competition of water and BTEX molecules for the same surface-active sites [51]. In contrast, Yan and co-workers found that humidity can improve the NO_2 sensing performance of

WS_2/graphene composites working at room temperature [66]. Shooshtari and co-workers observed an increase in the ethanol sensing response of TiO_2 nanowires for RH of up to 50% [73]. They explained that this behavior was a result of the presence of hydroxyl groups and oxygen adsorbates. For higher humidity levels (>50% RH), the hydroxyl groups cover almost all of the TiO_2 surface, thus limiting the oxygen adsorption and consequently reducing the sensitivity toward ethanol [73].

The SnZn2 sample was also evaluated to detect a reducing analyte, specifically CO gas, using the optimal temperature of 150 °C. Figure 8 shows that the same sample exhibited a very low sensitivity to CO gas. Despite detecting the CO gas, the sensing response of SnZn2 NPs toward NO_2 was superior compared to CO gas, as seen in Figure 8.

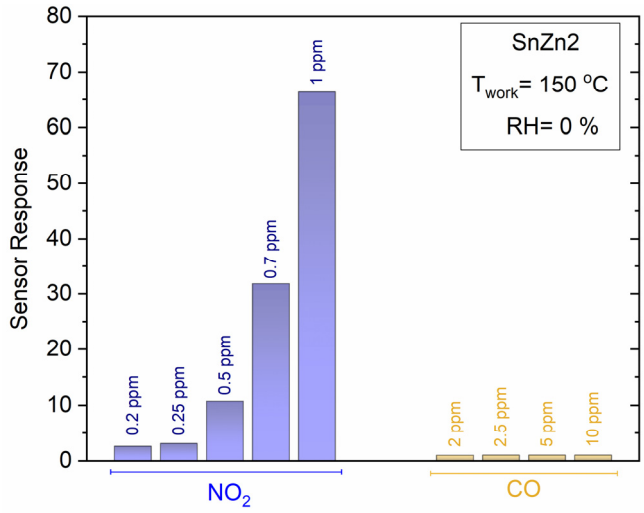

Figure 8. Comparison of the sensor response of SnZn2 exposed to NO_2 (0.2 to 1 ppm) and CO (2 to 10 ppm). These measurements were performed at 150 °C in a dry air atmosphere (0% RH).

It is clear that the results here obtained revealed that the addition of Zn ions into the SnO_2 nanocrystals significantly enhanced the sensing performance toward sub-ppm NO_2 levels. Nevertheless, it would be interesting in future works to find rational strategies to reduce the influence of moisture on gas sensitivity and to obtain a fair sensing performance (e.g., complete recovery, stability, and reproducibility) at working temperatures closer to room temperature.

4. Conclusions

We report here a versatile approach for preparing Zn-doped SnO_2 NPs via a microwave-assisted nonaqueous route for use as promising chemoresistive NO_2 sensors. XRD, XANES, and HRTEM analyses confirmed the presence of nanocrystalline SnO_2 and the absence of spurious phases. Sn-L edge XANES spectra revealed a local disorder around Sn atoms caused by the rapid crystallization provided by the microwave-assisted route. Zn-K edge XANES indicated that the Zn ions were incorporated into the SnO_2 network. XPS analyses revealed an increase in the oxygen defects at the SnO_2 surface, probably due to the partial replacement of Sn^{4+} by Zn^{2+} ions. The presence of these defects was linked to the high sensor response of SnZn2 (2 at% of Zn) toward NO_2 gas which was able to detect sub-ppm levels, i.e., from 0.1 ppm. Furthermore, the addition of Zn ions increased the moisture tolerance of SnO_2 NPs, presenting a higher sensing response in a more humid environment (40% RH) compared to a dry one. The enhanced sensor properties were linked to the presence of Zn ions that favored the formation of surface oxygen vacancies, thus contributing to the adsorption of NO_2 molecules. These findings highlight the promising properties of the microwave-assisted nonaqueous route for obtaining Zn-doped SnO_2 NPs for chemoresistive NO_2 sensors in practical applications.

Supplementary Materials: The following supporting information can be downloaded at: https://www.mdpi.com/article/10.3390/s24010140/s1, Figure S1: (a) Photograph of sensing platforms based on SnO_2 and SnZn2 samples compared to a U.S one tenth-dollar coin. (b) FESEM image of the SnZn2 sample onto sensing platform.; Figure S2: XPS spectra of the Zn-doped SnO_2 NPs synthesized via microwave-assisted route. (a) Survey scan, (b) Sn 3d and, (c) Zn 2p; Figure S3: NO_2 gas-sensing performance of SnZn2 nanocrystals kept at 150 °C and exposed to different relative humidity levels. (a) 0 %RH, (b) 20 %RH, and (c) 40 %RH. Ref. [74] is cited in S1. Preparation of sensing devices.

Author Contributions: Conceptualization, L.F.d.S.; Methodology, L.F.d.S. and M.A.L.; Formal analysis, L.F.d.S., M.A.L., A.C.C., W.A.J. and S.B.; Investigation, L.F.d.S. and M.A.L.; Writing—original draft, L.F.d.S., A.C.C. and S.B.; Writing—review & editing, L.F.d.S., M.A.L., A.C.C., W.A.J., S.B., K.A. and M.N.; Visualization, M.N.; Supervision, K.A., M.N. and E.L.; Project administration, E.L.; Funding acquisition, M.N. and E.L. All authors have read and agreed to the published version of the manuscript.

Funding: This was funded by FAPESP grant number [2015/20124-1, 2013/09573-3, 2013/07296-2 and 2022/02927-3] and CNPq grant number [442076/2014-2 and 405140/2018-5].

Informed Consent Statement: Not applicable.

Data Availability Statement: Data are contained within the article and supplementary materials.

Acknowledgments: This research was conducted during the internship of L. F. da Silva at the Laboratory for Multifunctional Materials (ETH Zürich, Switzerland). The internship was financially supported by FAPESP under grants No. 2015/20124-1 and 2013/09573-3. The Brazilian researchers thank the research funding institution CNPq (under grant No. 442076/2014-2 and 405140/2018-5), FAPESP (under grants 2013/07296-2 and 2022/02927-3), and CAPES for the financial support. XPS measurements and the fabrication of sensing platforms were conducted at the Brazilian Nanotechnology National Laboratory, LNNano, (Project LMF-24094 and XPS-18304), Campinas, SP, Brazil. Also, we appreciate the facilities (HRTEM) provided by LCE-UFSCar. This research used facilities of the Brazilian Synchrotron Light Laboratory (LNLS), part of the Brazilian Centre for Research in Energy and Materials (CNPEM), a private non-profit organization under the supervision of the Brazilian Ministry for Science, Technology, and Innovations (MCTI). The (XAFS2) beamline staff are acknowledged for their assistance during the experiments (XAFS2-20180311).

Conflicts of Interest: The authors declare that they have no known competing financial interests or personal relationships that could have appeared to influence the work reported in this paper.

References

1. Zhou, X.; Lee, S.; Xu, Z.; Yoon, J. Recent Progress on the Development of Chemosensors for Gases. *Chem. Rev.* **2015**, *115*, 7944–8000. [CrossRef] [PubMed]
2. Kampa, M.; Castanas, E. Human health effects of air pollution. *Environ. Pollut.* **2008**, *151*, 362–367. [CrossRef] [PubMed]
3. Dos Santos-Alves, J.S.G.; Patier, R.F. The environmental control of atmospheric pollution. The framework directive and its development. The new European approach. *Sens. Actuators B Chem.* **1999**, *59*, 69–74. [CrossRef]
4. Lin, S.-Y.; Ju, S.-W.; Lin, C.L.; Hsu, W.-H.; Lin, C.-C.; Ting, I.-W.; Kao, C.-H. Air pollutants and subsequent risk of chronic kidney disease and end-stage renal disease: A population-based cohort study. *Environ. Pollut.* **2020**, *261*, 114154. [CrossRef] [PubMed]
5. Yang, I.A.; Holz, O.; Jörres, R.A.; Magnussen, H.; Barton, S.J.; Rodríguez, S.; Cakebread, J.A.; Holloway, J.W.; Holgate, S.T. Association of Tumor Necrosis Factor-α Polymorphisms and Ozone-induced Change in Lung Function. *Am. J. Respir. Crit. Care Med.* **2005**, *171*, 171–176. [CrossRef] [PubMed]
6. Adamiec, E.; Jarosz-Krzemińska, E.; Bilkiewicz-Kubarek, A. Adverse health and environmental outcomes of cycling in heavily polluted urban environments. *Sci. Rep.* **2022**, *12*, 148. [CrossRef] [PubMed]
7. WHO/Health Topics/Air Pollution. Available online: https://www.who.int/health-topics/air-pollution#tab=tab_1 (accessed on 28 February 2020).
8. United States Environmental Protection Agency. Available online: https://www.epa.gov/no2-pollution/primary-national-ambient-air-quality-standards-naaqs-nitrogen-dioxide (accessed on 2 July 2022).
9. Abe, C.K.; Miraglia, G.S. Health Impact Assessment of Air Pollution in São Paulo, Brazil. *Int. J. Environ. Res. Public Health* **2016**, *13*, 694. [CrossRef]
10. Shendage, S.S.; Patil, V.L.; Vanalakar, S.A.; Patil, S.P.; Harale, N.S.; Bhosale, J.L.; Kim, J.H.; Patil, P.S. Sensitive and selective NO_2 gas sensor based on WO_3 nanoplates. *Sens. Actuators B Chem.* **2017**, *240*, 426–433. [CrossRef]
11. Casals, O.; Markiewicz, N.; Fabrega, C.; Gràcia, I.; Cané, C.; Wasisto, H.S.; Waag, A.; Prades, J.D. A Parts Per Billion (ppb) Sensor for NO_2 with Microwatt (μW) Power Requirements Based on Micro Light Plates. *ACS Sens.* **2019**, *4*, 822–826. [CrossRef]

12. Khomenko, S.; Pisoni, E.; Thunis, P.; Bessagnet, B.; Cirach, M.; Iungman, T.; Barboza, E.P.; Khreis, H.; Mueller, N.; Tonne, C.; et al. Spatial and sector-specific contributions of emissions to ambient air pollution and mortality in European cities: A health impact assessment. *Lancet Public Health* **2023**, *8*, 546–548. [CrossRef]
13. Li, Q.; Zeng, W.; Li, Y. Metal oxide gas sensors for detecting NO_2 in industrial exhaust gas: Recent developments. *Sens. Actuators B Chem.* **2022**, *359*, 131579. [CrossRef]
14. Zhang, F.; Lin, Q.; Han, F.; Wang, Z.; Tian, B.; Zhao, L.; Dong, T.; Jiang, Z. A flexible and wearable NO_2 gas detection and early warning device based on a spraying process and an interdigital electrode at room temperature. *Microsyst. Nanoeng.* **2022**, *8*, 40. [CrossRef]
15. Vallejos, S.; Stoycheva, T.; Umek, P.; Navio, C.; Snyders, R.; Bittencourt, C.; Llobet, E.; Blackman, C.; Moniz, S.; Correig, X. Au nanoparticle-functionalised WO_3 nanoneedles and their application in high sensitivity gas sensor devices. *Chem. Commun.* **2011**, *47*, 565–567. [CrossRef] [PubMed]
16. Miller, D.R.; Akbar, S.A.; Morris, P.A. Nanoscale metal oxide-based heterojunctions for gas sensing: A review. *Sens. Actuators B Chem.* **2014**, *204*, 250–272. [CrossRef]
17. Catto, A.C.; da Silva, L.F.; Bernardi, M.I.B.; Bernardini, S.; Aguir, K.; Longo, E.; Mastelaro, V.R. Local Structure and Surface Properties of $Co_xZn_{1-x}O$ Thin Films for Ozone Gas Sensing. *ACS Appl. Mater. Interfaces* **2016**, *8*, 26066–26072. [CrossRef] [PubMed]
18. Gurlo, A. Nanosensors: Does Crystal Shape Matter? *Small* **2010**, *6*, 2077–2079. [CrossRef] [PubMed]
19. Naresh, B.; Krishna, K.G.; D, R.; Kuchi, C.; Kummara, S.K.; Reddy, P.S. Synthesis and characterization of rGO wrapped 1-D NiO nanofibers for ammonia gas sensing application. *Surf. Interfaces* **2023**, *40*, 103012. [CrossRef]
20. Korotcenkov, G.; Cho, B.K. Spray pyrolysis deposition of undoped SnO_2 and In_2O_3 films and their structural properties. *Prog. Cryst. Growth Charact. Mater.* **2017**, *63*, 1–47. [CrossRef]
21. Annanouch, F.E.; Haddi, Z.; Ling, M.; Di Maggio, F.; Vallejos, S.; Vilic, T.; Zhu, Y.; Shujah, T.; Umek, P.; Bittencourt, C.; et al. Aerosol-Assisted CVD-Grown PdO Nanoparticle-Decorated Tungsten Oxide Nanoneedles Extremely Sensitive and Selective to Hydrogen. *ACS Appl. Mater. Interfaces* **2016**, *8*, 10413–10421. [CrossRef]
22. Li, X.; Lu, D.; Shao, C.; Lu, G.; Li, X.; Liu, Y. Hollow $CuFe_2O_4/\alpha$-Fe_2O_3 composite with ultrathin porous shell for acetone detection at ppb levels. *Sens. Actuators B Chem.* **2018**, *258*, 436–446. [CrossRef]
23. Kucharski, S.; Ferrer, P.; Venturini, F.; Held, G.; Walton, A.S.; Byrne, C.; Covington, J.A.; Ayyala, S.K.; Beale, A.M.; Blackman, C. Direct in situ spectroscopic evidence of the crucial role played by surface oxygen vacancies in the O_2-sensing mechanism of SnO_2. *Chem. Sci.* **2022**, *13*, 6089–6097. [CrossRef]
24. Wu, W.; Liao, L.; Zhang, S.; Zhou, J.; Xiao, X.; Ren, F.; Sun, L.; Dai, Z.; Jiang, C. Non-centrosymmetric Au–SnO_2 hybrid nanostructures with strong localization of plasmonic for enhanced photocatalysis application. *Nanoscale* **2013**, *5*, 5628–5636. [CrossRef] [PubMed]
25. Zahmatkeshani, F.; Tohidi, M. Synthesis of SnO_2, Zn-doped SnO_2 and Zn_2SnO_4 nanostructure-based hierarchical architectures by using deep eutectic precursors and their photocatalytic application. *CrystEngComm* **2019**, *21*, 6758–6771. [CrossRef]
26. Periyasamy, M.; Kar, A. Modulating the properties of SnO_2 nanocrystals: Morphological effects on structural, photoluminescence, photocatalytic, electrochemical and gas sensing properties. *J. Mater. Chem. C* **2020**, *8*, 4604–4635. [CrossRef]
27. Mishra, S.R.; Ahmaruzzaman, M. Tin oxide based nanostructured materials: Synthesis and potential applications. *Nanoscale* **2022**, *14*, 1566–1605. [CrossRef] [PubMed]
28. da Silva, G.T.S.T.; Lopes, O.F.; Catto, A.C.; Patrocinio, A.O.T.; Rodrigues, J.E.F.S.; Mesquita, A.; Ribeiro, C.; Avansi Jr, W.; da Silva, L.F. Long-and short-range structure of SnO_2 nanoparticles: Synthesis and photo(electro)catalytic activity. *Mater. Chem. Phys.* **2023**, 127989. [CrossRef]
29. Zhang, S.; Jia, X.; Geng, Q.; He, Z.; Hu, Y.; Gao, Y.; Yang, S.; Yao, C.; Zhang, Q.; Wang, D.; et al. Solvent engineering of SnO_2 electron transport layer for high-performance perovskite solar cells. *Surf. Interfaces* **2023**, *41*, 103226. [CrossRef]
30. Vallejos, S.; Selina, S.; Annanouch, F.E.; Gràcia, I.; Llobet, E.; Blackman, C. Aerosol assisted chemical vapour deposition of gas sensitive SnO_2 and Au-functionalised SnO2 nanorods via a non-catalysed vapour solid (VS) mechanism. *Sci. Reports* **2016**, *6*, 28464. [CrossRef]
31. Mudra, E.; Shepa, I.; Milkovic, O.; Dankova, Z.; Kovalcikova, A.; Annušová, A.; Majkova, E.; Dusza, J. Effect of iron doping on the properties of SnO_2 nano/microfibers. *Appl. Surf. Sci.* **2019**, *480*, 876–881. [CrossRef]
32. Kou, X.; Wang, C.; Ding, M.; Feng, C.; Li, X.; Ma, J.; Zhang, H.; Sun, Y.; Lu, G. Synthesis of Co-doped SnO_2 nanofibers and their enhanced gas-sensing properties. *Sens. Actuators B Chem.* **2016**, *236*, 425–432. [CrossRef]
33. Babaie, A.; Rezaei, M.; Sofla, R.L.M. Investigation of the effects of polycaprolactone molecular weight and graphene content on crystallinity, mechanical properties and shape memory behavior of polyurethane/graphene nanocomposites. *J. Mech. Behav. Biomed. Mater.* **2019**, *96*, 53–68. [CrossRef] [PubMed]
34. Shooshtari, M.; Vollebregt, S.; Vaseghi, Y.; Rajati, M.; Pahlavan, S. The sensitivity enhancement of TiO_2-based VOCs sensor decorated by gold at room temperature. *Nanotechnology* **2023**, *34*, 255501. [CrossRef] [PubMed]
35. Xu, F.; Li, W.; Sun, S.; Zhong, A.; Cheng, X.; Shi, J.; Li, Z.; Li, J.; Zhang, W.; Wang, X.; et al. Expanding Selectivity Functionality of a ZnO Nanotetrapod-Based Volatile Organic Compound Sensor Using Au Nanoparticle Decoration. *ACS Appl. Nano Mater.* **2023**, *6*, 8335–8345. [CrossRef]

36. Vallejos, S.; Umek, P.; Stoycheva, T.; Annanouch, F.; Llobet, E.; Correig, X.; De Marco, P.; Bittencourt, C.; Blackman, C. Single-Step Deposition of Au- and Pt-Nanoparticle-Functionalized Tungsten Oxide Nanoneedles Synthesized Via Aerosol-Assisted CVD, and Used for Fabrication of Selective Gas Microsensor Arrays. *Adv. Funct. Mater.* **2013**, *23*, 1313–1322. [CrossRef]
37. Wang, W.; Liu, Y.; Liu, S. SnO_2 Nanostructure with Well-Engineered Crystal Facets by Zn Doping for Chemical Sensing Applications. *Cryst. Growth Des.* **2020**, *20*, 2742–2752. [CrossRef]
38. Zhao, Q.; Deng, X.; Ding, M.; Gan, L.; Zhai, T.; Xu, X. One-pot synthesis of Zn-doped SnO_2 nanosheet-based hierarchical architectures as a glycol gas sensor and photocatalyst. *CrystEngComm* **2015**, *17*, 4394–4401. [CrossRef]
39. Tammanoon, N.; Wisitsoraat, A.; Tuantranont, A.; Liewhiran, C. Flame-made Zn-substituted SnO_2 nanoparticulate compound for ultra-sensitive formic acid gas sensing. *J. Alloys Compd.* **2021**, *871*, 159547. [CrossRef]
40. Sun, P.; You, L.; Sun, Y.; Chen, N.; Li, X.; Sun, H.; Ma, J.; Lu, G. Novel Zn-doped SnO_2 hierarchical architectures: Synthesis, characterization, and gas sensing properties. *CrystEngComm* **2012**, *14*, 1701–1708. [CrossRef]
41. Wang, W.; Tian, Y.; Li, X.; Wang, X.; He, H.; Xu, Y.; He, C. Enhanced ethanol sensing properties of Zn-doped SnO_2 porous hollow microspheres. *Appl. Surf. Sci.* **2012**, *261*, 890–895. [CrossRef]
42. Baraneedharan, P.; Imran Hussain, S.; Dinesh, V.P.; Siva, C.; Biji, P.; Sivakumar, M. Lattice doped Zn–SnO_2 nanospheres: A systematic exploration of dopant ion effects on structural, optical, and enhanced gas sensing properties. *Appl. Surf. Sci.* **2015**, *357*, 1511–1521. [CrossRef]
43. Somacescu, S.; Ghica, C.; Simion, C.E.; Kuncser, A.C.; Vlaicu, A.M.; Stefan, M.; Ghica, D.; Florea, O.G.; Mercioniu, I.F.; Stanoiu, A. Nanoclustered Pd decorated nanocrystalline Zn doped SnO_2 for ppb NO_2 detection at low temperature. *Sens. Actuators B Chem.* **2019**, *294*, 148–156. [CrossRef]
44. Niederberger, M. Nonaqueous Sol–Gel Routes to Metal Oxide Nanoparticles. *Acc. Chem. Res.* **2007**, *40*, 793–800. [CrossRef] [PubMed]
45. Bilecka, I.; Niederberger, M. Microwave chemistry for inorganic nanomaterials synthesis. *Nanoscale* **2010**, *2*, 1358–1374. [CrossRef] [PubMed]
46. da Silva, L.F.; Catto, A.C.; Avansi, W.; Mesquita, A.; Maia, L.J.Q.; Lopes, O.F.; Li, M.S.; Moreira, M.L.; Longo, E.; Andrés, J.; et al. Unveiling the efficiency of microwave-assisted hydrothermal treatment for the preparation of $SrTiO_3$ mesocrystals. *Phys. Chem. Chem. Phys.* **2019**, *21*, 22031–22038. [CrossRef] [PubMed]
47. da Silva, L.F.; Lucchini, M.A.; M'Peko, J.-C.; Bernardini, S.; Aguir, K.; Ribeiro, C.; Longo, E.; Niederberger, M. ZnO/SnO_2 Heterojunctions Sensors with UV-Enhanced Gas-Sensing Properties at Room Temperature. *Proceedings* **2017**, *1*, 418.
48. Michalowicz, A.; Moscovici, J.; Muller-BouvetDiane, D.; Provost, K. MAX: Multiplatform Applications for XAFS. *J. Phys. Conf. Ser.* **2009**, *190*, 12034.
49. de Palma, J.V.N.; Catto, A.C.; de Oliveira, M.C.; Ribeiro, R.A.P.; Teodoro, M.D.; da Silva, L.F. Light-assisted ozone gas-sensing performance of SnO_2 nanoparticles: Experimental and theoretical insights. *Sens. Actuators Rep.* **2022**, *4*, 100081. [CrossRef]
50. da Silva, L.F.; M'Peko, J.-C.; Catto, A.C.; Bernardini, S.; Mastelaro, V.R.; Aguir, K.; Ribeiro, C.; Longo, E. UV-enhanced ozone gas sensing response of ZnO-SnO_2 heterojunctions at room temperature. *Sens. Actuators B Chem.* **2017**, *240*, 573–579. [CrossRef]
51. da Silva, L.F.; Catto, A.C.; Bernardini, S.; Fiorido, T.; de Palma, J.V.N.; Avansi, W.; Aguir, K.; Bendahan, M. BTEX gas sensor based on hematite microrhombuses. *Sens. Actuators B Chem.* **2021**, *326*, 128817. [CrossRef]
52. de Mendonça, V.R.; Avansi, W.; Arenal, R.; Ribeiro, C. A building blocks strategy for preparing photocatalytically active anatase TiO_2/rutile SnO_2 heterostructures by hydrothermal annealing. *J. Colloid Interface Sci.* **2017**, *505*, 454–459. [CrossRef]
53. Avansi Jr., W.; Ribeiro, C.; Leite, E.R.; Mastelaro, V.R. Vanadium Pentoxide Nanostructures: An Effective Control of Morphology and Crystal Structure in Hydrothermal Conditions. *Cryst. Growth Des.* **2009**, *9*, 3626–3631. [CrossRef]
54. Dalmaschio, C.J.; Ribeiro, C.; Leite, E.R. Impact of the colloidal state on the oriented attachment growth mechanism. *Nanoscale* **2010**, *2*, 2336–2345. [CrossRef] [PubMed]
55. de Mendonca, V.R.; Dalmaschio, C.J.; Leite, E.R.; Niederberger, M.; Ribeiro, C. Heterostructure formation from hydrothermal annealing of preformed nanocrystals. *J. Mater. Chem. A* **2015**, *3*, 2216–2225. [CrossRef]
56. Liu, Z.; Handa, K.; Kaibuchi, K.; Tanaka, Y.; Kawai, J. Comparison of the Sn L edge X-ray absorption spectra and the corresponding electronic structure in Sn, SnO, and SnO_2. *J. Electron Spectros. Relat. Phenom.* **2004**, *135*, 155–158. [CrossRef]
57. Perelshtein, I.; Ruderman, E.; Perkas, N.; Tzanov, T.; Beddow, J.; Joyce, E.; Mason, T.J.; Blanes, M.; Mollá, K.; Patlolla, A.; et al. Chitosan and chitosan–ZnO-based complex nanoparticles: Formation, characterization, and antibacterial activity. *J. Mater. Chem. B* **2013**, *1*, 1968–1976. [CrossRef] [PubMed]
58. Da Silva, L.F.; Lopes, O.F.; Catto, A.C.; Avansi, W.; Bernardi, M.I.B.; Li, M.S.; Ribeiro, C.; Longo, E. Hierarchical growth of ZnO nanorods over SnO_2 seed layer: Insights into electronic properties from photocatalytic activity. *RSC Adv.* **2016**, *6*, 2112–2118. [CrossRef]
59. Chen, Y.; Duan, X.; Zhou, X.; Wang, R.; Wang, S.; Ren, N.; Ho, S.-H. Advanced oxidation processes for water disinfection: Features, mechanisms and prospects. *Chem. Eng. J.* **2021**, *409*, 128207. [CrossRef]
60. Wagner, T.; Valbusa, D.; Bigiani, L.; Barreca, D.; Gasparotto, A.; Maccato, C. XPS characterization of Mn_2O_3 nanomaterials functionalized with Ag and SnO_2. *Surf. Sci. Spectra* **2020**, *27*, 24004. [CrossRef]
61. Epifani, M.; Prades, J.D.; Comini, E.; Pellicer, E.; Avella, M.; Siciliano, P.; Faglia, G.; Cirera, A.; Scotti, R.; Morazzoni, F.; et al. The Role of Surface Oxygen Vacancies in the NO_2 Sensing Properties of SnO_2 Nanocrystals. *J. Phys. Chem. C* **2008**, *112*, 19540–19546. [CrossRef]

62. Brinzari, V.; Cho, B.K.; Kamei, M.; Korotcenkov, G. Photoemission surface characterization of (001) In_2O_3 thin film through the interactions with oxygen, water and carbon monoxide: Comparison with (111) orientation. *Appl. Surf. Sci.* **2015**, *324*, 123–133. [CrossRef]
63. Al-Hashem, M.; Akbar, S.; Morris, P. Role of Oxygen Vacancies in Nanostructured Metal-Oxide Gas Sensors: A Review. *Sens. Actuators B Chem.* **2019**, *301*, 126845. [CrossRef]
64. Marikutsa, A.; Rumyantseva, M.; Konstantinova, E.A.; Gaskov, A. The Key Role of Active Sites in the Development of Selective Metal Oxide Sensor Materials. *Sensors* **2021**, *21*, 2554. [CrossRef] [PubMed]
65. Blackman, C. Do We Need "Ionosorbed" Oxygen Species? (Or, "A Surface Conductivity Model of Gas Sensitivity in Metal Oxides Based on Variable Surface Oxygen Vacancy Concentration"). *ACS Sens.* **2021**, *6*, 3509–3516. [CrossRef] [PubMed]
66. Yan, W.; Worsley, M.A.; Pham, T.; Zettl, A.; Carraro, C.; Maboudian, R. Effects of ambient humidity and temperature on the NO_2 sensing characteristics of WS_2/graphene aerogel. *Appl. Surf. Sci.* **2018**, *450*, 372–379. [CrossRef]
67. Jeng, C.-C.; Chong, P.J.H.; Chiu, C.-C.; Jiang, G.-J.; Lin, H.-J.; Wu, R.-J.; Wu, C.-H. A dynamic equilibrium method for the SnO_2-based ozone sensors using UV-LED continuous irradiation. *Sens. Actuators B Chem.* **2014**, *195*, 702–706. [CrossRef]
68. Alagh, A.; Annanouch, F.E.; Al Youssef, K.; Bittencourt, C.; Güell, F.; Martínez-Alanis, P.R.; Reguant, M.; Llobet, E. PdO and PtO loaded WS_2 boosts NO_2 gas sensing characteristics at room temperature. *Sens. Actuators B Chem.* **2022**, *364*, 131905. [CrossRef]
69. Degler, D.; Wicker, S.; Weimar, U.; Barsan, N. Identifying the Active Oxygen Species in SnO_2 Based Gas Sensing Materials: An Operando IR Spectrsocopy Study. *J. Phys. Chem. C* **2015**, *119*, 11792–11799. [CrossRef]
70. Gherardi, S.; Zonta, G.; Astolfi, M.; Malagù, C. Humidity effects on SnO_2 and $(SnTiNb)O_2$ sensors response to CO and two-dimensional calibration treatment. *Mater. Sci. Eng. B* **2021**, *265*, 115013. [CrossRef]
71. Hernández-Ramírez, F.; Tarancón, A.; Casals, O.; Arbiol, J.; Romano-Rodríguez, A.; Morante, J.R. High response and stability in CO and humidity measures using a single SnO_2 nanowire. *Sens. Actuators B Chem.* **2007**, *121*, 3–17. [CrossRef]
72. Yang, J.; Han, W.; Jiang, B.; Wang, C.; Sun, Y.; Zhang, H.; Shimanoe, K.; Sun, P.; Lu, G. Sn^{2+} doped NiO hollow nanofibers to improve triethylamine sensing characteristics through tuning oxygen defects. *Sens. Actuators B Chem.* **2023**, *387*, 133801. [CrossRef]
73. Shooshtari, M.; Salehi, A.; Vollebregt, S. Effect of temperature and humidity on the sensing performance of TiO_2 nanowire-based ethanol vapor sensors. *Nanotechnology* **2021**, *32*, 325501. [CrossRef] [PubMed]
74. Hilaire, S.; Suess, M.J.; Kranzlin, N.; Bienkowski, K.; Solarska, R.; Augustynski, J.; Niederberger, M. Microwave-assisted nonaqueous synthesis of WO_3 nanoparticles for crystallographically oriented photoanodes for water splitting. *J. Mater. Chem. A* **2014**, *2*, 20530–20537.